Using Molecular Dynamics To Simulate Electronic Spin Resonance Spectra of T4 Lysozyme

Ileana Stoica[†]

488 Rhodes Hall, Cornell University, Ithaca, New York 14850

Received: July 20, 2003; In Final Form: October 12, 2003

The stochastic Liouville formalism (SLE) allows for electronic spin resonance (ESR) spectra to be computed for proteins and lipids, using a stochastic model for the motion of the nitroxide spin probe. The present work reports a molecular dynamics (MD) study of spin-labeled T4 lysozyme, where information extracted from the atomically detailed trajectories is used within the framework of the Liouville equation. Sets of 10 MD trajectories, with two force fields, were produced for each of the T4 mutants N40C and K48C, previously used in ESR experiments. Fluctuations of the local relevant degrees of freedom, order parameters for the spin probe, free induction decay profiles, and finally high-field ESR line shapes were calculated for the two proteins. Sampling probabilities for the nitroxide rotational degrees of freedom are in agreement with the traditional model of Brownian rotational diffusion in a restricting potential. Present results suggest that improved sampling (longer time scale, more averaging over initial conditions) is needed for a reliable multicomponent fitting to experimental spectra from molecular dynamics trajectories.

1. Introduction

Electron paramagnetic resonance is a powerful spectroscopical method that enables the analysis of relatively fast (down to less than one nanosecond) processes at the molecular level. Recent advances of EPR such as multi-frequency EPR allow for probing of complex dynamics in biomolecules; using very high-frequencies spectra,[1−3] fast snapshots of molecular motions are captured (such as localized backbone and side-chain fluctuations), whereas slow snapshots (9 GHz) obtained with low-field ESR give information on the global motions (e.g., protein tumbling). Recent developments of the technique (two-dimensional FT-ESR, high magnetic field EPR experiments[1]) have made it possible to probe aspects of the protein dynamics at the level of fast, localized fluctuations of the protein backbone.[1−6] The shorter (as compared to NMR) relaxation time of the excited electron enables the study of relatively fast (subnanosecond) processes; therefore, local spin probe dynamics effectively modulates the electron spin Hamiltonian, making EPR spectra more sensitive to local motions.[1−6] Single-cysteine spin-labeled mutants of T4 lysozyme have been the focus of a series of beautiful experiments and simulations aimed at understanding the nature of differences in side chain motions, using the spin probe as a reporter of local dynamics.[7−9] The use of doubly labeled T4 lysozyme mutants has been proved successful for probing functionally relevant domain motions in T4 lysozyme, such as the hinge-bending motion.[10]

Aside from T4 lysozyme, other proteins' dynamics have been studied by SDSL in combination with EPR, some experiments being accompanied by investigations of local nitroxide motions by molecular dynamics simulations; light-dependent motions in rhodopsin have been mapped using measurements of dipole−dipole interactions from EPR spectra,[11−13] electron-transfer processes in the photosynthetic reaction centers have been investigated from spin polarized transient ESR spectra,[14−17] and motions of the myosin regulatory domain, needed to produce mechanical force upon muscle contraction, have been characterized from ESR spectra of spin-labeled myosin.[18] However, EPR spectra for proteins in solution were not computed within a theoretical formalism, from first principles, or by making explicit use of atomically detailed molecular dynamics information. A first application of the Liouville equation formalism combined with the use of molecular dynamics to generate atomically detailed trajectories on a lipid system was reported in the study of Hakansson et al.[19]

Considerable work was done in the past on developing a theoretical framework for the calculation of EPR line shapes. Any approach to deriving EPR spectra for biomolecules has to account for the coupling between the internal molecular motions (modeled as classical degrees of freedom) and the relaxation of the electron spin (quantum-mechanical degrees of freedom), and more specifically, to provide realistic models of the spin probe dynamics.

A formalism that yields remarkably accurate fits to experimental data is the stochastic Liouville equation (SLE) of Freed and co-workers.[20−23] In the stochastic Liouville equation the model is of a spin Hamiltonian coupled to a few spatial (and diffusive) degrees of freedom. The all-protein motion is modeled as rigid-body diffusion, whereas the other two types of motions are described as Brownian rotational diffusion in an orienting potential. The parameters of the model are selected to best fit the experimental data. The advantage is the relative ease of analysis and simulations. The model was applied with impressive success to the study of proteins, membranes and nucleic acids.[2−4,8,28,29]

Other approaches[24−27,30] use Brownian dynamics (BD) simulations to provide the input, in the form of real-time trajectories, to the stochastic Liouville equation. In other studies slow-motion EPR spectra were calculated by using BD simulations of lipids in a reorienting potential ("diffusion in a cone"[25,27]) and also by including translational diffusion on curved surfaces.[26]

An independent and complementary view of the probe and protein motions is given by molecular dynamics simulations;

† E-mail: istoica@physics.cornell.edu.
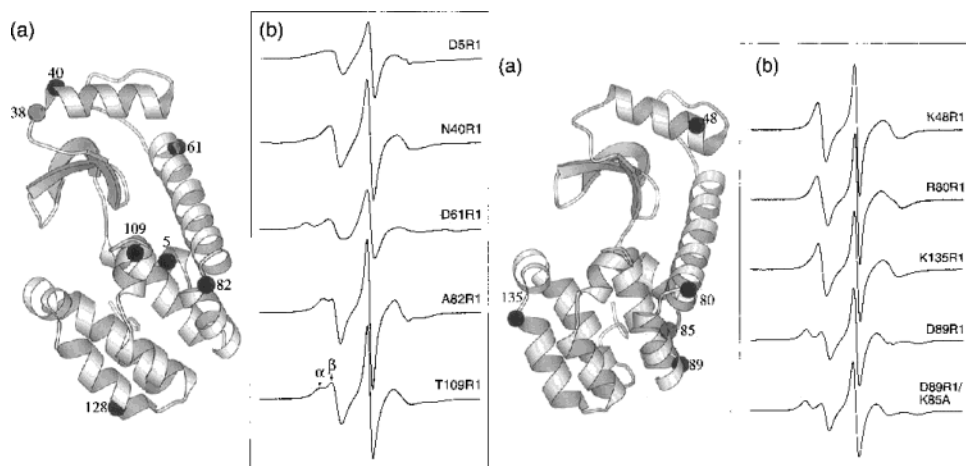
Figure 1. (a) Crystal structure of T4L showing the location of helix N-terminal sites (left) and the location of the C-terminal sites (right). (b) Corresponding EPR spectra of side-chain R1. Figure reproduced from ref 7.

the time scale of picoseconds to nanoseconds, required to probe local chain fluctuations and spin label motions, is adequate for the use of molecular dynamics; in addition, trajectories provide atomic detail on the protein, nitroxide probe (especially interesting for analyzing the local fluctuations), as well as on interactions between the labeled protein and the solvent. Molecular dynamics trajectories of labeled lipids have already been used[19] to solve the Liouville equation and obtain free induction decay (FID) profiles; the need for total trajectory times larger than what was attainable with molecular dynamics (100 ns in the study of Hakansson et al.,[19] led to the extrapolation of the molecular dynamics FID by using a "flexible BD model".[19]

The goal of the present work is to use the information provided by molecular dynamics to modulate the electronic spin Hamiltonian by a spin-probe orientation-dependent component, to time-evolve the spin density matrix following the equation above, and to finally compute EPR spectra. Also, extending the computation to make use of the whole ensemble of trajectories, and averaging over protein initial orientations, are parts of the computational procedure. The resulting EPR line shapes should accurately predict the position and width of peaks as obtained from experimental studies[7−9] and should be sensitive to local degrees of mobility. The starting point is the stochastic Liouville equation (SLE) formalism.[20−23] The dynamic description of the classical degrees of freedom, in the form of Euler angles $\Omega(t)$, is included in the SLE together with the quantum mechanical spin degrees.[20−23] In the SLE formalism, in addition to a spin Liouville operator L, a classical operator Γ acts on the spin density matrix ρ, describing the stochastic time-dependence of the spin−lattice coupling:

$$\frac{d\rho(\Omega,t)}{dt} = -i[L(t),\rho(\Omega,t)] + \Gamma\rho(\Omega,t) \qquad (1)$$

The first SLE approaches were based on expressing the orientational probability distribution $P(\Omega,t)$ in terms of eigenfunctions of Γ ("the eigenfunction expansion"). The task then became to develop dynamic models of Markov processes causing the stochastic time dependence of the spin−lattice coupling. One common model is Brownian rotational diffusion of a rigid body in a restricting potential. The line shape $I(\omega)$ is the Fourier transform of the trajectory-averaged spin magnetization, taken with the appropriate equilibrium distribution over orientations $P_0(\Omega)$:

$$I(\omega) = \int_0^{+\infty} e^{-i\omega t} \int P_0(\Omega)\langle M(\Omega,t)\rangle \, d\Omega \, dt \qquad (2)$$

where the average $\langle...\rangle$ is performed over spin degrees of freedom, Euler angles, and number of trajectories. One alternative approach to coupling the spin degrees of freedom to molecular motion consists of explicitly taking the dynamics of the classical degrees of freedom $\Omega(t)$ in the form of trajectories, and solving the following Liouville equation:[27−30]

$$\frac{d\rho_{spin}(\Omega(t),t)}{dt} = -\frac{i}{\hbar}[H_{spin}(\Omega(t),t),\rho_{spin}((\Omega(t),t)] \qquad (3)$$

2. Method

2.1. Molecular Dynamics Simulations. EPR spectra of proteins are frequently measured using one or multiple nitroxide probes attached to the protein molecule. The spin label is conveniently linked to a cysteine residue via a sulfur bridge. The cysteine may be native, or a result of site-directed mutagenesis. The site-directed spin labeling (SDSL) technique has become increasingly powerful for analyzing EPR spectra of spin-labeled proteins in terms of a set of variables that describe the local environment of the spin label, and are dependent on the protein fold at the attachment site.[7−9]

A series of ESR experiments have focused on T4 lysozyme and a variety of its cysteine mutants. In these experiments, as a function of the spin label position along the protein backbone, features of the EPR line shapes were indicative of various degrees of backbone flexibility, even at sites where the tertiary structure and degree of solvent exposure were very similar.[7−9]

In Figure 1 are presented results extracted from the work of Mchaourab et al.,[7] in particular, the results of the experiments aimed at comparing and contrasting helix N- and C-terminal sites.

In the present work, the two T4 lysozyme variants chosen are spin labeled at the N-terminus and C-terminus of the T4 lysozyme B-helix (N40−K48), respectively.

The R1 probe has been widely used in EPR experiments on variants of T4 lysozyme.[7−10] An energy function of the probe was designed using an ab initio method and empirically available parameters. The geometry of the ring was optimized using Gaussian with 6-31+G** basis functions. The partial charges on the ring atoms were computed by using RESP from the Amber package for charge fitting to reproduce the electric field.[31] The parameters for the initial geometry of the molecule were taken from similar chemical groups (pyrrole).

To extract the time series of spin label orientations, sets of 10 molecular dynamics trajectories per lysozyme mutant were

ESR Spectra of T4 Lysozyme

J. Phys. Chem. B, Vol. 108, No. 5, 2004 **1773**
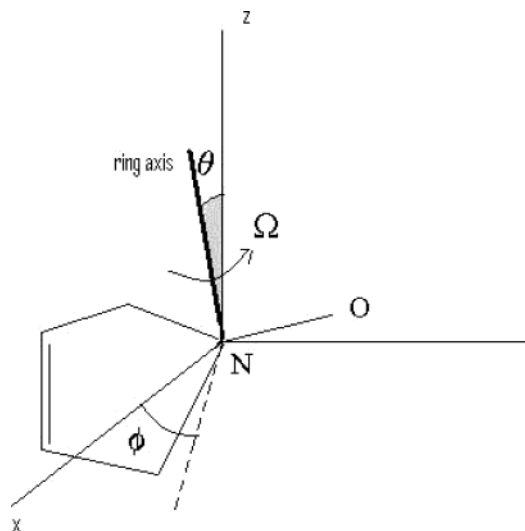
Figure 2. Rotational degrees of freedom Ω, θ, ϕ describing the motion of the spin probe ring axis e in the laboratory frame.

produced, with two different force fields, using the molecular dynamics package MOIL of Elber et al.[32]

The two lysozyme variants were embedded in a water box of 60A filled with TIP3 water molecules, with periodic boundary conditions. After the standard "bad contact" run at 10 K (for 20 ps), heating to 300 K (60 ps), followed by 100 ps equilibration, the production runs were started. A total of 10 trajectories per mutant, between 5.5 ns and 6 ns each, were simulated with the OPLS/AMBER force field,[33] using the group LINUX cluster and the Cornell Theory Center Windows 2000 cluster. As a force field sensitivity check to local (spin probe) motions, a second set of 3 ns trajectories, 10 per lysozyme mutant, were also generated using the AMBER99[34] force field parameters, which were implemented in the MOIL simulation package. Ewald summation[35] was used to account for long-range electrostatics, and a 10 Å cutoff radius was used for the direct sum; the cutoff for the van der Waals interactions was 9 Å. Bonds were constrained using the SHAKE algorithm. Velocities were initially sampled from a Maxwell distribution and were tested for rescaling (to fit room temperature) every 2 ps. The time step used in the Verlet algorithm was 2 fs; coordinates were saved every 0.2 ps. The motion of the nitroxide label was analyzed in both the laboratory frame (where the magnetic field B_0 is aligned with the z-axis), and the protein-fixed reference frame, where protein rotation was removed. Protein translation was suppressed during the simulations by applying a harmonic potential ($k = 5$ kcal mol^{-1} Å^{-2}) to constrain the center of mass translation. For analyzing the local motions (at the level of spin probe atoms), the procedure described by Kabsch[36] was used. The relevant quantity in this procedure is the rotation matrix $\mathbf{U}(t)$, which best overlaps a given coordinate subset to the initial coordinates (reference structure), at a given time point.[36] The atoms selected for this calculation were the R1 ring atoms. The ring structure was checked for planarity during the course of the simulations. In addition, the coordinates of the nitrogen and oxygen atoms can be extracted for analysis of the NO-bond vector fluctuations. The rotation angles Ω, θ, and ϕ sampled by the nitroxide label along the trajectory can be computed from the trace of the rotation matrix and the components of e, the probe axis vector (Figure 2).

2.2. Electron Spin Hamiltonian. The nitroxide electron spin Hamiltonian describes the Zeeman energy and the hyperfine coupling between the electron and the ^{14}N nucleus. In fact, as a result of a Gaussian optimization run, the electron was found

to be localized with 0.6 Mulliken spin density on the ^{14}N nucleus, the rest of the probability density residing on the oxygen atom. The total spin Hamiltonian includes the isotropic Hamiltonian, the anisotropic part, and the Hamiltonian describing the applied pulse:[20−24]

$$H_{\text{spin}}(t) = H_{\text{iso}} + H_1 + V(t) = S_z g_{\text{iso}} \mathbf{B}_0 + S_z A_{\text{iso}} I_z + H_1 + \\ H_{xy} \cos(\omega_x t) \quad (4)$$

$\mathbf{B}_0$ represents the static magnetic field of the spectrometer and scales with the resonance frequency ω_0. The isotropic magnetic and hyperfine constants are defined as follows:

$$g_{\text{iso}} = \frac{g_{xx} + g_{yy} + g_{zz}}{3} \qquad A_{\text{iso}} = \frac{A_{xx} + A_{yy} + A_{zz}}{3} \quad (5)$$

$\mathbf{S}$ and $\mathbf{I}$ are the electronic and nuclear spin operators, respectively. H_{xy} is the Hamiltonian describing the perturbing field, applied in the xy-plane. In the present work a $(\pi/2)_x$ pulsed experiment is simulated, in which the time-dependent magnetic field that induces the transitions is turned on for a short duration of time and then is turned off. The signal in the time domain is obtained by following the relaxation of the magnetization to equilibrium, or the free induction decay (FID). The EPR spectrum is the Fourier transform of this signal. The simulation starts after the perturbation is turned off; therefore H_{xy} is zero. Instead, the initial conditions (at time 0+) correspond to a $M(t=0) = -(M_y)$ magnetization.

Time dependence is implicit in H_1; the anisotropic Hamiltonian H_1 is dependent on the rotational degrees of freedom of the spin label, which in turn are time-dependent. The coupling between the spin degrees of freedom (treated quantum mechanically) and the "bath" (nitroxide moiety, protein, solvent) degrees of freedom (treated classically) is a consequence of the anisotropy of the magnetic tensors; this, in turn, arises from the coupling between the electron angular momentum, which depends on the spatial coordinates, and the electron spin. The anisotropic part of the spin Hamiltonian contains scalar products of two second-rank tensors: the magnetic tensor $\tilde{g}$ and the hyperfine tensor $\tilde{A}$, in the form

$$H_1(t) = \mathbf{S}\Delta\tilde{g}\mathbf{B}_0 + \mathbf{S}\Delta\tilde{A}\mathbf{I} \quad (6)$$

It is usually assumed[25−27] that the principal axes of both tensors $\tilde{g}$ and $\tilde{A}$ coincide; the same assumption was used here. While the $\tilde{g}$ and $\tilde{A}$ tensors are diagonalized in the spin probe frame (or molecular frame) (Figure 3), which reorients together with the spin probe molecule, the spin operators are quantized in the laboratory frame:

The connection between the two frames has been made in the current work by using the following two alternative approaches.

2.2.1. Irreducible Tensor Method. The orientation-dependent part of the spin Hamiltonian $H_1(\Omega(t))$ is expressed in terms of products of irreducible tensors:[19−22]

$$H_1(t) = H_1^g(t) + H_1^A(t) = \sum_{\mu=g,A} \sum_M F_{\mu,\text{lab}}^{(L,M)*} A_{\mu,\text{lab}}^{(L,M)} \quad (7)$$

where $\mu = g$, A represents the Zeeman and the hyperfine part of the Hamiltonian, respectively, $F_\mu^{(L,M)*}$'s are the magnetic tensors, and $A_\mu^{(L,M)}$'s correspond to electronic and nuclear spin operators. However, the magnetic tensors $\mathbf{F}$ are given in the molecular frame, whereas the spin operators A are given in the
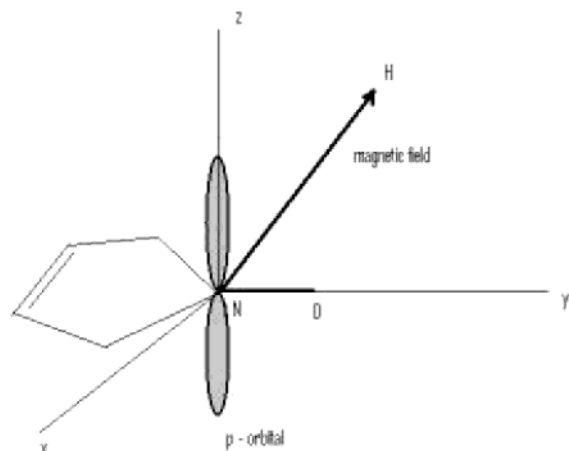
Figure 3. Molecular (spin probe-attached) frame, qualitative representation (values of magnetic tensor components are used from experiment[8]).

laboratory frame. Hence, to compute H_1, the magnetic tensors need to be transformed from the molecular to the laboratory frame. Here the Wigner matrices or generalized spherical harmonics are introduced, such that the magnetic tensors expressed in the molecular frame $F_{\mu,\text{molec}}^{(L,M)*}$ transform to the laboratory frame $F_{\mu,\text{lab}}^{(L,M)*}$ according to

$$F_{\mu,\text{lab}}^{(L,M)*} = \sum_K F_{\mu,\text{molec}}^{(L,K)*} \, D_{M,K}^L(\Omega) \qquad (8)$$

Because the irreducible tensors that appear in the spin Hamiltonian are second-rank tensors, $L = 2$; the other quantum numbers K and M are restricted by $|M| \leq L$, $|K| \leq L$. Therefore, the final form of the spin Hamiltonian expressed in terms of products of the magnetic tensors, given in the molecular frame, and spin operator tensors, in the laboratory frame, is[19−22]

$$H_1(t) = \sum_{\mu=(g,A)} \sum_{\text{M,K}} F_{\mu,\text{molec}}^{(2,K)*} \, D_{M,K}^2(\Omega) A_{\mu,\text{lab}}^{(2,M)} \qquad (9)$$

The time-dependent variable denoted generically as $\Omega(t)$ is the triplet $\alpha(t)$, $\beta(t)$, $\gamma(t)$ of Euler angles describing the orientation of the nitroxide frame relative to the laboratory frame.

In the present work, the nitroxide Euler angles are extracted from the MD trajectories: they are computed from the time series of rotation matrices $\mathbf{U}(t)$ as described previously and are denoted by $\Omega(t)$, $\theta(t)$, and $\Phi(t)$. The rotation matrices are extracted in the laboratory frame; that is, there is no model for the protein rotation, which would result in an additional sum in the spin Hamiltonian, with Wigner matrices of the type $D_{K,N}^2(\Omega_{\text{prot}}(t))$. Instead, averaging over initial conditions is performed by considering a series of initial tile angles (protein axis tilt angles), equally spaced between 0 and 180°. These initial angles appear only in the lowest order, i.e., in Wigner matrices $D_{0,0}^2(\theta_{\text{prot}}(t))$.

The components of the irreducible magnetic tensors and spin operators are given in the Appendix.

To further simplify the computation of the spin Hamiltonian, the model proposed by Freed[38] for slow-tumbling spectra of nitroxides is used. In addition, terms involving the $S_z I_\pm$ products, which are responsible for the singly forbidden transitions, are left out in a first attempt to produce simple test-case spectra. Therefore, the nucleus is assumed to be in an eigenstate ($I_z =$

−1, 0, or +1); this is a reasonable approximation at high fields, where the hyperfine interaction is significantly smaller than the electron Zeeman term (which scales with the applied z field) but becomes a problem for low-field simulations, causing differences from experimental spectra. In this simplified picture, which still keeps the dimensionality of the problem 2 (for the spin density matrix and spin Hamiltonian, as will be discussed below), the first term in the anisotropic spin Hamiltonian contains a

$$D_{0,0}{}^2 \sim \frac{3\cos^2(\theta) - 1}{2} \qquad (10)$$

type of dependence on the angle θ between the spatial direction of the electron orbital and the direction of the static magnetic field. The second term in the anisotropic spin Hamiltonian contains the Wigner matrix elements:

$$D_{0,2}{}^2 + D_{0,-2}{}^2 \sim \sin^2(\theta) \cos(2\phi) \qquad (11)$$

dependent on the ϕ rotation angle, in addition to θ.

2.2.2. Rotation Matrices. The translation between the laboratory frame and the molecular frame (where magnetic tensors are diagonalized) can also be done using rotation matrices $\mathbf{U}(t)$, extracted directly from the simulation data (as described previously):

$$H_1(t) = \mathbf{S}\mathbf{U}^{\text{T}}(t) \, \Delta\tilde{g}\mathbf{U}(t)\mathbf{B}_0 + \mathbf{S}\mathbf{U}^{\text{T}}(t) \, \Delta\tilde{A}\mathbf{U}(t)\mathbf{I} \qquad (12)$$

The electronic $\mathbf{S}$ and nuclear $\mathbf{I}$ spin operators are here defined as x, y, z vectors and so is the magnetic field $\mathbf{B}_0$. The 3×3 rotation matrices are Hermitian and orthogonal, with a +1 determinant. As with the Wigner matrix method, the procedure is exact. The two methods should be directly translatable one into the other, both accomplishing the transformation of second rank tensors (the magnetic tensors) from one representation (molecular frame tensors in their irreducible forms) to another (laboratory frame).

A final issue is that of averaging over initial conditions. Initial protein rotation matrices $\mathbf{V}$ have been computed, describing either random orientations (created with random numbers such that the matrices are Hermitian and unitary) or gradual tilt angles from 0 to 180°, time-independent in both cases. Initial conditions are incorporated into the Hamiltonian by replacing $\mathbf{U}(t)$ with $\mathbf{V}\mathbf{U}(t)$; both matrices are defined ($\mathbf{V}$) or computed ($\mathbf{U}$) in the absolute (laboratory) frame.

2.3. Solving the Liouville Equation. The experimental observable, the magnetization, and its Fourier transform, the line shape, are computed directly from the spin density matrix:

$$M_{xy}(t) = \text{Trace}[(M_x + iM_y)\rho(t)] \qquad (13)$$

The real part of the Fourier transform gives the absorptive spectrum (which is the one of interest). The trace is computed over the spin and the spatial coordinates.

The principal task then becomes to solve the Liouville equation for the spin density matrix:

$$\frac{d\rho}{dt} = -\frac{i}{\hbar}[H,\rho] = -\frac{i}{\hbar}(H\rho - \rho H) \qquad (14)$$

The equation is of low dimensionality (two electron spin degrees of freedom); therefore, ρ is a 2×2 matrix of complex numbers. To filter out oscillations corresponding to the static magnetic field (ω_0), analysis of the free induction decay (FID) has been done in the interaction picture; i.e., the Liouville equation is

ESR Spectra of T4 Lysozyme

J. Phys. Chem. B, Vol. 108, No. 5, 2004 **1775**
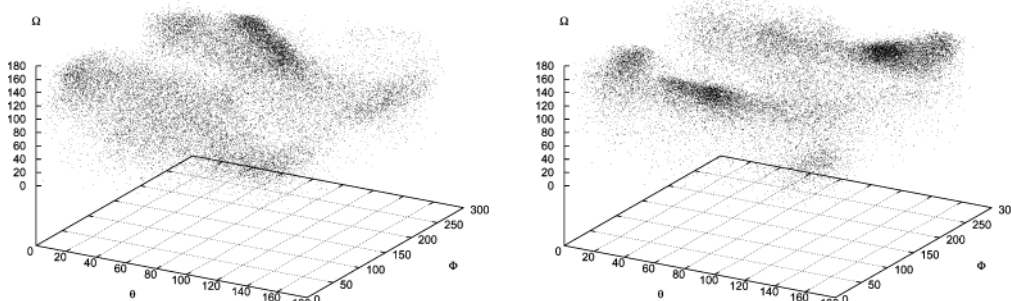
Figure 4. Sampling of the rotational degrees of freedom, from 5.5 ns molecular dynamics trajectories, for N40C (left) and K48C (right). OPLS/AMBER force field simulations.
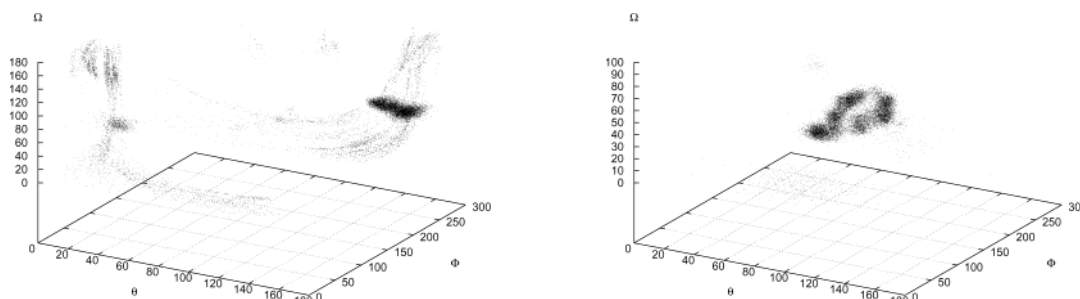
Figure 5. Sampling of the rotational degrees of freedom, from 3 ns molecular dynamics trajectories, for N40C (left) and K48C (right). AMBER force field trajectories.

solved for a transformed density matrix ρ_R:

$$\rho_R = R\rho R^{-1} \tag{15}$$

where the matrix **R** is

$$\mathbf{R} = e^{i\omega_0 t} \tag{16}$$

The result is the removal of the $\omega_0 S_z$ term describing oscillations at the frequency of the static field. In the interaction picture, it was found that for propagating the density matrix, a Runge–Kutta algorithm in the fourth order gave good numerical stability. Currently, both the spin Hamiltonian and the spin density matrix are 2×2 matrices, expressed in the space of the spin eigenstates. This treatment is based on the underlying assumption that the nitrogen nucleus is in one of its $I_z = -1, 0, +1$ eigenstates, motivated by the difference between the electronic and nuclear masses. In low-field experiments especially, mixing of the spin and nuclear eigenstates occurs. In this case, terms accounting for singly forbidden transitions, $I_{\pm}S_z$, become important in the spin Hamiltonian; therefore, a more appropriate space to work in for simulating low-field spectra is the 36-dimensional space of electron and nuclear eigenstates, or a relevant subspace (e.g., 9-dimensional[25−27]).

3. Results

3.1. Analysis of Spin Probe Motion. The first issue addressed is the sampling of the Euler angle space by the spin probe. A total of 10 trajectories per mutant have been analyzed with the OPLS/AMBER force field simulations, and 5 AMBER force field trajectories per mutant have been analyzed for comparison. The EPR spectra have been generated using the OPLS/AMBER trajectories, but a force field sensitivity check using the AMBER force field can point out potential sampling issues and future directions for the improvement of spectra. Figure 4 shows sample plots of the 3 rotation angles Ω, θ, and ϕ, for N40C and K48C, extracted from OPLS/AMBER trajectories. A dot in any of these plots is an actual value of the $(\Omega,$

θ, $\phi)$ triplet sampled by the spin probe during one 5.5 ns molecular dynamics trajectory. The sets of rotation matrices used for EPR spectra calculations are in direct relation to the triplets (Ω, θ, ϕ) represented in Figure 4 (even though all 10 trajectories have been analyzed, only one trajectory per mutant is shown as an example).

The existence of at least two high-density states is more apparent in the AMBER trajectories, even though most often these local minima are not equally populated; there might be an issue of insufficient sampling, the total trajectory time being only 3 ns in the AMBER force field simulations, instead of 5.5 ns in the OPLS/AMBER trajectories (Figure 5).Unidirectional projections of the 3D-probability density have also been calculated; the angle of interest is here θ, between the probe axis and the laboratory z-axis (magnetic field). The normalization is done with respect to the number of data points, and to the size of the θ-bin (3 degrees in this case). Averages over 9 OPLS/AMBER trajectories have been performed (Figure 6). In the OPLS/AMBER trajectories, there are differences in $P(\theta)$ probability densities between one mutant and the other, mainly concerning the bimodal character of the probability density profile, which is more pronounced in the K48C trajectories. A bimodal profile of the $P(\theta)$ histogram indicates jumping between two preferred states (discrete orientations), in agreement with the suggested model for spin probe diffusion.[8,24]

The AMBER force field trajectories show a more pronounced bimodal character (especially for N40C) as compared to the OPLS/AMBER trajectories; trajectory averages exhibited multiple peaks (results not shown), indicating that sampling might be incomplete on the 3 ns time scale of the AMBER simulations. Given computation time and storage considerations, the AMBER trajectories were not further extended, or used in the actual simulation of ESR spectra. They served as a reference and showed the dependency of spin probe degrees of freedom on the force field used.

3.2. Local Fluctuations. Mean square fluctuations (MSF) for the B-helix residues can be computed from the molecular
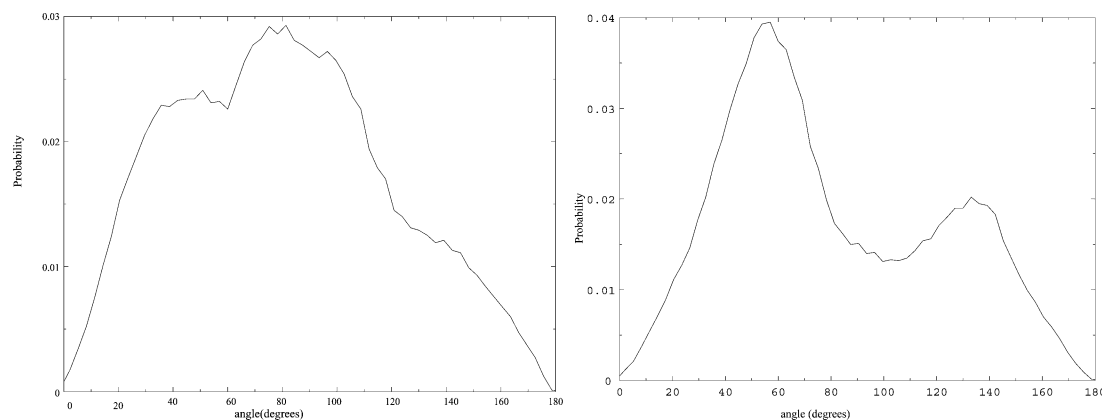
Figure 6. Probability density of θ angle sampling; average over nine 5.5 ns OPLS/AMBER molecular dynamics trajectories of N40C (left) and K48C (right).
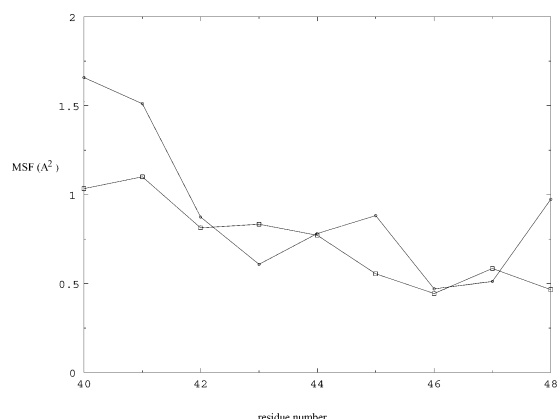
Figure 7. C_α mean square fluctuations MSF along the B-helix, predicted from the first 1 ns of a N40C molecular dynamics trajectory corrected for protein motion (circles) and from the crystallographic *B*-factors (squares).

dynamics trajectories and compared to the crystallographic *B*-factors via

$$B_i = \frac{8\pi^2 MSF}{3} = \frac{8\pi^2 \langle [\mathbf{r}_i(t) - \langle \mathbf{r}_i \rangle]^2 \rangle_t}{3} \qquad (17)$$

T4 lysozyme *B*-factors for the B-helix residues (C_α atoms) are shown in Figure 7. It is important to note that both the molecular dynamics trajectory and the crystallographic *B*-factors indicate more thermal motion for the N-terminus of the B-helix than for the C-terminus.

Root-mean-square deviations of the spin probe ring atoms have also been computed, in a protein-fixed reference frame, and have been found to have similar amplitudes in the two T4

variants (Figure 8). The relevant local degrees of freedom consist of the set of[7–10] the Euler angles describing the ring axis position with respect to the magnetic field, the torsion angles χ_1 to χ_5 about the rotatable bonds that link R1 and the CYS residue, and the Euler angles that describe the orientation of the B-helix axis in the laboratory frame (backbone motions). Torsion angles were easily computed using a MOIL routine, and the B-helix axis was computed as the eigenvector corresponding to the smallest eigenvalue of the B-helix moment of inertia tensor (backbone atoms only).

Autocorrelation functions were computed according to the formula

$$C(\tau) = \frac{1}{n} \langle \cos(\theta(t)) \cos(\theta(t+\tau)) \rangle_{t=n\delta t} \qquad (18)$$

For variations in rotation angles. e.g.,

$$\delta\theta = \theta(t+\delta t) - \theta(t) \qquad (19)$$

a sine correlation function was calculated, thus eliminating constant terms from the Taylor expansion:

$$\mathrm{corr}_{\sin}(\tau) = \frac{1}{n} \langle \sin(\delta\theta(t)) \sin(\delta\theta(t+\tau)) \rangle_{t=n\delta t} \qquad (20)$$

Autocorrelations of the spin probe Euler angles exhibit a fast (tens of picoseconds) decay, corresponding to an inertial motional regime, followed by a nanosecond scale diffusive decay (with incomplete decay in the AMBER trajectories due to insufficient sampling). The decay profiles were similar in both mutants (θ, analysis shown below) (Figures 9 and 10). In both the OPLS/AMBER and the AMBER force field simulations, for all three spin probe Euler angles, the variations within
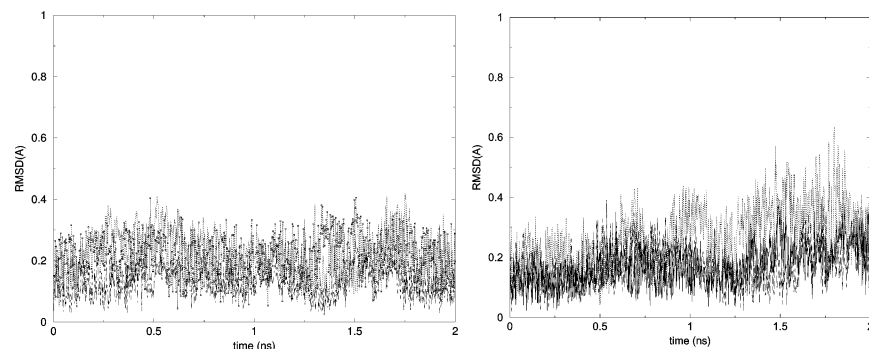

Figure 8. Root-mean-square deviation (rmsd) of R1 ring atoms in 2 ns of molecular dynamics, in a protein-fixed reference frame, three selected trajectories, N40C (left) and K48C (right).

ESR Spectra of T4 Lysozyme

J. Phys. Chem. B, Vol. 108, No. 5, 2004 **1777**
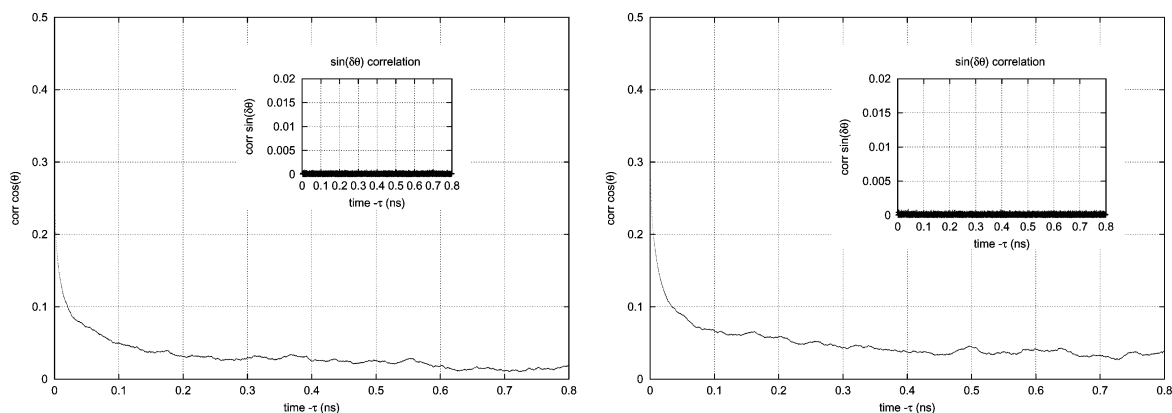
Figure 9. Autocorrelation functions of the θ angle and for variations of θ within one time step (0.2 ps); average over nine 5.5 ns trajectories of N40C (left) and K48C (right). OPLS/AMBER trajectories.
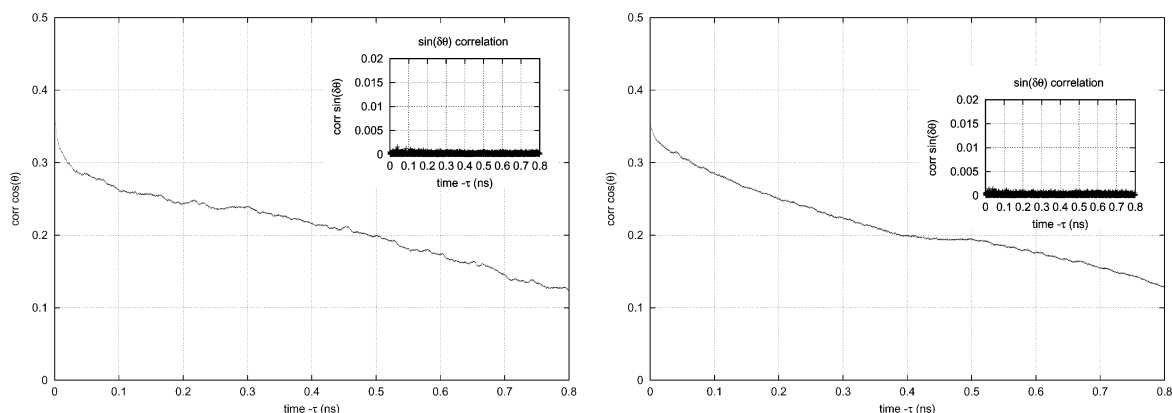
Figure 10. Autocorrelation functions of the θ angle and for variations of θ within one time step (0.15 ps); average over five 3 ns trajectories of N40C (left) and K48C (right). AMBER trajectories.
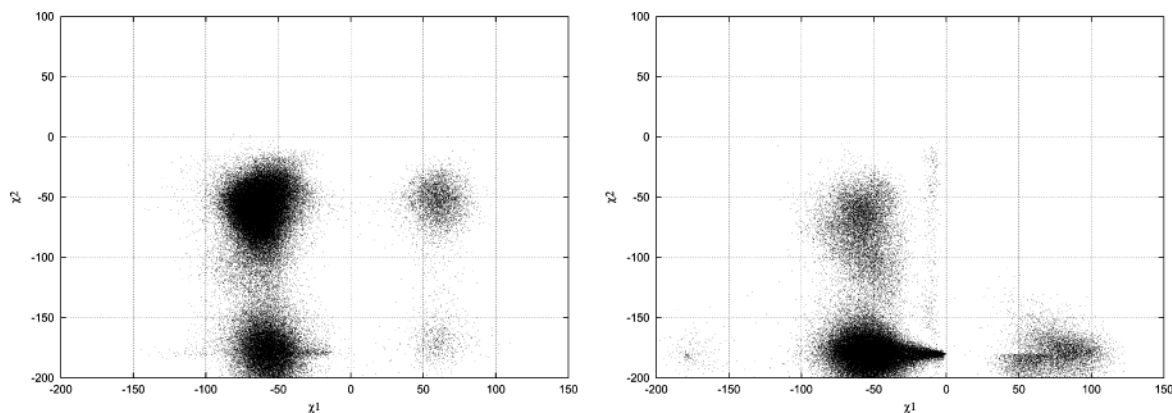

Figure 11. Torsion angle analysis in mutant N40C (left) and K48C (right). Trajectories 3, 5, and 6 (total of 13 ns) corrected for protein motion used for analysis.

one time step were highly uncorrelated, which is an indication of the randomness of the nitroxide motion (angular velocities), on the time scale considered (0.2 and 0.15 ps, respectively). The result is in agreement with previous descriptions of the spin label motion as Brownian diffusion in an orienting potential.[8,24]

Essential in the EPR line shape interpretation is identifying the torsional restrictions at each site, and correlating them with the presence/absence of immobilized EPR components.[8-10] An analysis of the χ_1 and χ_2 torsion angle population from the OPLS/AMBER simulations indicated that the preferred rotameric states in both mutants were those expected for weakly ordered sites (Figure 11). There was no indication of a restriction in the torsional angle sampling for N40C as opposed to K48C, which in experiment gave rise to a supplemental immobilized component in N40C.[7] This result could be a consequence of

the weak interactions of the sulfide atoms with the helix backbone and is common for both force fields (AMBER results not shown).

The backbone fluctuations at the labeling site, resulting from helix axis rotations or from twisting about the helix axis, have been proposed to be determining factors of local mobilities, and of EPR line shapes.[8-10] The final purpose of this analysis was to describe backbone fluctuations, such as the motion of the N40−K48 helix axis, and to investigate the coupling between backbone fluctuations and spin probe reorientations. Due to more complete sampling, the OPLS/AMBER trajectories have been used for this type of analysis. The helix axis motion was studied in the space of rotation angles. Joint probability distributions for the helix degrees of freedom and torsion angles have been analyzed. The high-probability regions (from analysis of several
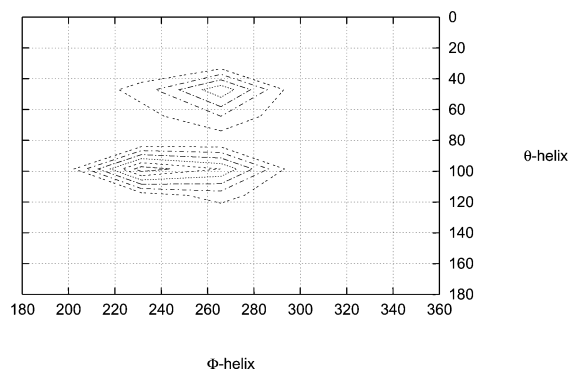
Figure 12. B-helix motion in the laboratory frame. Joint probability density for the helix axis θ and Φ angles, on a 12° grid; N40C, trajectory 5.

trajectories) indicate that the helix axis has one, at most two preferred states, which might support the existing model of diffusion in a cone, with jumps between two distinct cone axis positions (Figure 12).[8-10] Correlations between torsions and the R1 Euler angles, and between torsions and the B-helix motions, which have been proposed from ESR studies:

$$\frac{\langle\cos(\chi_{4,5}(t))\cos(\theta_{spin},\Omega_{spin}(t))\rangle - \langle\cos(\chi_{4,5}(t))\rangle\langle\cos(\theta_{spin},\Omega_{spin}(t))\rangle}{\text{RMSD}(\cos(\chi_{4,5}(t)))\,\text{RMSD}(\cos(\theta_{spin},\Omega_{spin}(t)))} \tag{21}$$

and

$$\frac{\langle\cos(\chi_{4,5}(t))\cos(\theta_{helix},\Omega_{helix}(t))\rangle - \langle\cos(\chi_{4,5}(t))\rangle\langle\cos(\theta_{helix},\Omega_{helix}(t))\rangle}{\text{RMSD}(\cos(\chi_{4,5}(t)))\,\text{RMSD}(\cos(\theta_{helix},\Omega_{helix}(t)))} \tag{22}$$

have been found consistently close to zero in the present analysis, for either of the two mutants.

As a conclusion to this section, the analysis of local fluctuations points out the lack of correlations between R1 and side-chain or backbone motions, and the Brownian-like character of the probe rotations, on the time scale probed by the MD simulation (0.2 ps).

3.3. Time-Domain Signal; Computation of Free Induction Decay (FID). *3.3.1. Discussion of the Procedure.* Free induction decay has been simulated using both the expansion of the Hamiltonian in Wigner matrices, and the molecular dynamics extracted rotation matrices. The procedure is the following: The anisotropic spin Hamiltonian is computed using both approaches discussed in the Methods. The Liouville equation for the electron spin density matrix is then solved; the solution is propagated with a 0.2 ps time step, for a total time of 55 or 110 ns, if appended sets of rotation matrices were used, extracted from OPLS/AMBER molecular dynamics trajectories. If simple cases were considered such as a fixed-angle spectrum or a powder spectrum, no molecular dynamics information was necessary and the total time scale could be increased to 200 or 400 ns (which was found to be enough for accurately reproducing the position of peaks and the line widths). Finally, the FID was examined back in the laboratory frame. The sets of rotation matrices from individual 5.5 ns trajectories have been appended to obtain trajectories closer to the time scales necessary for observing a fully decayed FID. In other words, rather than considering an ensemble average of the spin density matrix over all trajectories, with an equilibrium distribution, it was assumed that equilibrium is attained for each 5.5 ns trajectory, and that

considering an extended 55 ns (or multiples of 55 ns) trajectory is equivalent to taking a time average of the spin density matrix.

Two basic assumptions are made with this procedure:

1. The spin probe reaches equilibrium within the time necessary for one molecular dynamics trajectory.

2. The dependence of the sampling probability on the initial conditions for each single trajectory is not significant. If this dependence were strong and different 5 ns trajectories explored substantially different regions of the Euler angle space, depending on how "remote" (in rmsd terms) the initial structures were, then the resulting "appended" trajectory would artifactually exhibit high-probability regions that would not correspond to local energy minima of one true 10 ns trajectory. Both problems have been addressed. In the OPLS/AMBER trajectories, the correlation of the rotation angles decays within one nanosecond, and the 3D-sampling profiles in the Euler angle space do not qualitatively show differences in the distribution of the dots (triplets of angles sampled at each time point) after the first 2−3 ns. This indicates that equilibration in the space of rotational degrees of freedom is reached by the end of an individual trajectory.

Second, at least in the OPLS/AMBER simulations, from analysis of all 10 trajectories for each variant, it was found that the starting conditions were not a significant factor in the sampling of the rotational degrees of freedom: As part of the molecular dynamics setup described in the Methods, the initial structures for the 10 trajectories per mutant were selected as frames, 10 ps apart, of one 1 ns initial molecular dynamics production run. Therefore, trajectories with consecutive numbers were started from structures 10 ps one from the other. However, the differences between the 3D rotation angle sampling profiles between consecutive trajectories were found comparable to the ones between trajectories started from initial conditions 100 ps apart. This indicated that initial conditions were not essential in determining the extent of Euler angle space sampled by the end of the trajectory.

From the quantity

$$\text{Trace}[U(t)\,U^{\text{T}}(t+\delta t)] \tag{23}$$

"jumps" in the values of Euler angles, in one step ($\delta t = 0.2$ ps) can also be analyzed. As a last check on the validity of the method, the trace of the rotation matrix has been analyzed on a 55 ns trajectory resulting from appending all individual trajectories.[37] The absence of high "jumps" in the trace of the rotation matrix product $\mathbf{U}(t)\,\mathbf{U}^{\text{T}}(t+\text{d}t)$ in the vicinity of "points of appendage" has been interpreted as an argument in favor of the appending procedure.[37]

Likewise, the reorientational correlation function $g(t)$ and order parameters S have also been found not to vary substantially in single versus appended trajectories and, moreover, not to depend on the order in which trajectories were appended.

In the conditions described above, the resulting high-field (250 GHz) FID, with averaging over protein tilt angles, has the form given in Figure 13.

3.3.2. Order Parameters. Molecular dynamics may be better suited (and more effective in bringing new information) to simulate high-field spectra, due to its picosecond temporal resolution, which makes it possible to effectively probe fast dynamic modes through coupling of the electron spin to the spin label molecular motions, which in turn are coupled to the protein local environment (backbone fluctuations). An important quantity for assessing the time scale of (T_2-type) intrinsic

ESR Spectra of T4 Lysozyme

J. Phys. Chem. B, Vol. 108, No. 5, 2004 **1779**
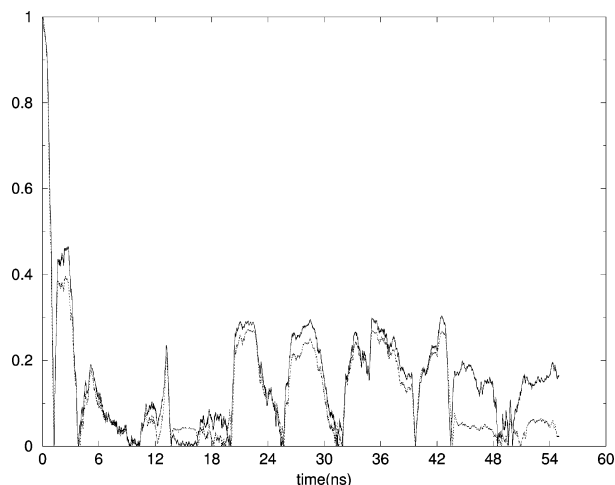
Figure 13. 250 GHz FID signal, computed on a 55 ns MD trajectory of N40C, with 10 (solid line) and 20 (dotted line) protein tilt angles between 0 and 90° and 0 and 180°, respectively. Rotation matrix method.

relaxation processes in the system, for the case of high-field spectra, is the reorientational correlation function, defined as

$$g(t) = \langle P_2(\cos(\theta(t) - \theta(t_0))) \rangle \equiv \sum_n \langle D_{n0}^{2*}[\Omega(t)] \, D_{n0}^2[\Omega(t_0)] \rangle \tag{24}$$

Second-order Wigner matrix elements $D_{n0}^2(\Omega(t))$, where $\Omega(t)$ is, in conformity with the standard notation,[20-27] the triplet (Ω, θ, ϕ) sampled during the molecular dynamics trajectory, are extracted from rotation matrices $\mathbf{U}(t)$. The computation of $g(t)$, which involves averages over initial times, has been done on an extended 110 ns trajectory in rotation angle space (obtained as described previously). The reorientational correlation function $g(t)$ exhibits a faster (subnanosecond) decay, followed by a slower, nanosecond time scale decay (full decay is not achieved in 10ns, in either of the mutants) (Figure 14). An ordering tensor can be defined:

$$S_{\alpha\beta} = \langle (3l_\alpha l_\beta - \delta_{\alpha\beta})/2 \rangle \tag{25}$$

where α and β are molecular axes of the spin label and l_α is the cosine between the α axis and the director $\mathbf{n}$. The irreducible tensor components are

$$S_0 = S_{zz} \qquad S_1 = \sqrt{\frac{1}{3}\left(S_{zz} - \frac{S_{xx} + S_{yyy}}{2}\right)}$$

$$S_2 = \sqrt{\frac{2}{3}}(S_{xx} - S_{yy}) \tag{26}$$

The irreducible components of $\tilde{S}$, or order parameters, can be obtained as time averages:

$$S_0 = \langle |D_{00}^{2*}[\Omega(t)]|^2 \rangle$$

$$S_1 = \langle |D_{10}^{2*}[\Omega(t)]|^2 \rangle$$

$$S_2 = \langle |D_{20}^{2*}[\Omega(t)]|^2 \rangle$$

The order parameters were calculated for single trajectories as well as for the appended trajectories, from rotation matrices extracted from the trajectory of R1 in the laboratory frame, as well as in the protein-fixed frame; differences in order-parameter values were in the second decimal. Average values for the
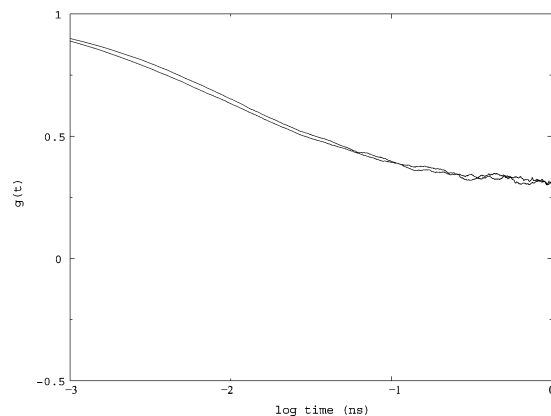
Figure 14. $g(t)$ reorientational correlation functions plotted 110 ns trajectories of N40C (solid line) and K48C (dotted line), obtained by appending pieces of 5.5 ns MD trajectories; logarithmic scale.

order parameters in N40C were

$$S_0 = 0.23 \qquad S_1 = 0.19 \qquad S_2 = 0.19 \tag{27}$$

In K48C, the order parameters, as extracted from the 110 ns trajectory, were

$$S_0 = 0.20 \qquad S_1 = 0.22 \qquad S_2 = 0.17 \tag{28}$$

The computed order parameters correspond to weakly ordered sites, in agreement with the results from torsional angle analysis. The formula used to compute order parameters is exact only in the case of axially symmetric magnetic tensors, which is not the case in the present study. Therefore, the small differences in the order parameters between the two mutants cannot be further exploited to infer differences in actual mobilities, with the exception of S_0, which is only dependent on the tilt angle θ. Given that the trajectory-averaged sampling probabilities $P(\theta)$ (Figure 6) are also different in the two mutants, the equivalent time-averaged information contained in S_0 may indicate an actual slightly higher flexibility in N40C.

3.4. EPR Spectra. When simulating EPR spectra, two test cases were considered: fixed-angle spectra and powder spectra. The following values were used for the components of the magnetic tensor (in frequency units) and hyperfine tensor (in Gauss):

$$g_{xx} = 2.00814 \qquad g_{yy} = 2.00597 \qquad g_{zz} = 2.00221 \tag{29}$$

$$A_{xx} = 6.18 \qquad A_{yy} = 5.70 \qquad A_{zz} = 36.20 \tag{30}$$

The $\tilde{g}$ and $\tilde{A}$ tensor components are slightly dependent upon the site at which the nitroxide probe is attached.[8] Because no available data were found for the particular N40 and K48 sites, values found in ref 8 were used.

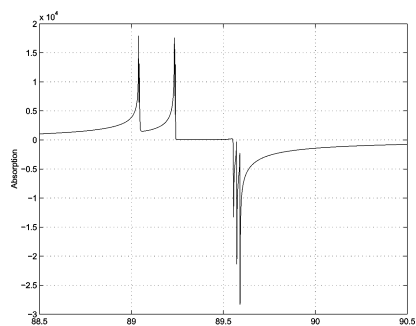From the irreducible tensor method, the predicted g shift is

$$\Delta g = \frac{2}{3}\left(g_{zz} - \frac{g_{xx} + g_{yy}}{2}\right)\frac{3\cos^2(\theta) - 1}{2}\omega_0 +$$
$$(g_{xx} - g_{yy})\sin^2(\theta)\cos(2\Phi)\omega_0 \tag{31}$$
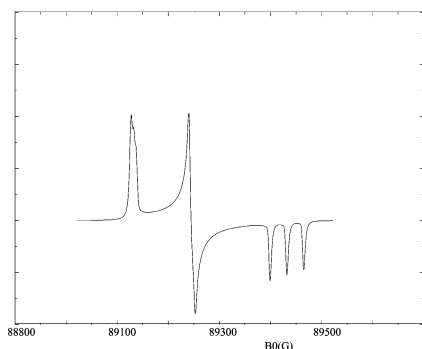
and the peak-to-peak distance is equal to

$$A_{iso} + \frac{2}{3}\left(A_{zz} - \frac{A_{xx} + A_{yy}}{2}\right)\frac{3\cos^2(\theta) - 1}{2} +$$
$$(A_{xx} - A_{yy})\sin^2(\theta)\cos(2\Phi) \tag{32}$$
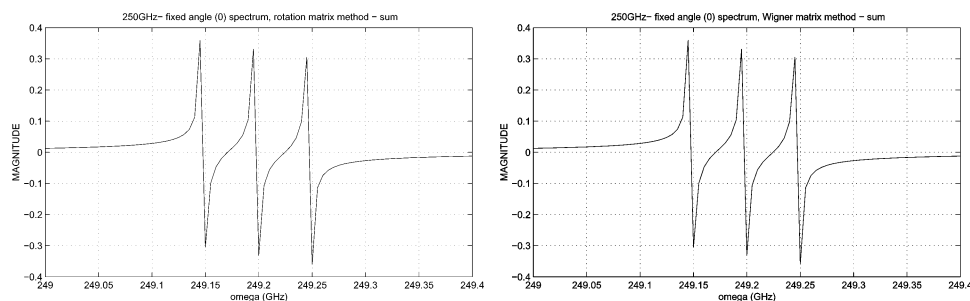
Figure 15. 250 GHz EPR spectrum obtained from a 200 ns FID (no MD information): rotation matrix method (left) and Wigner method (right).


Figure 16. 250 GHz powder spectrum obtained from a 400 ns FID. Rotation matrix method.

Figure 17. 250 GHz powder spectrum simulated with the NSSL package (Freed et al.).

For a simple test case (fixed 0° angle), the expected *g* shift at 250 GHz is approximately −0.8 GHz (to the left of ω_0), and the peak-to-peak distance is 0.05 GHz.

The simulated fixed-angle lines have the expected nitroxide signature form and correspond to the calculated peak positions and splitting (Figure 15). The other simple case to test is the "powder spectrum", with averaging over many (2000) tilt angles, equally incremented between 0 and 180° (rotations about both *x* and *y* axes) (Figure 16). For comparison, a high-field rigid limit powder spectrum was simulated for nitroxide using the software package developed in Jack Freed's group. The same $\tilde{g}$ and $\tilde{A}$ components were used as for all other simulations, an
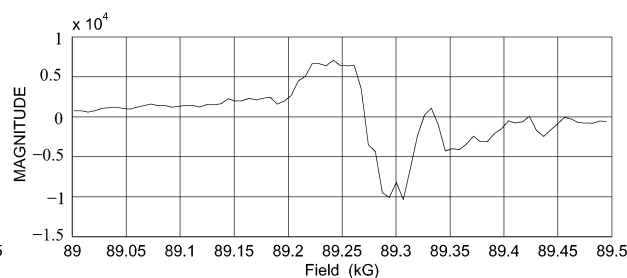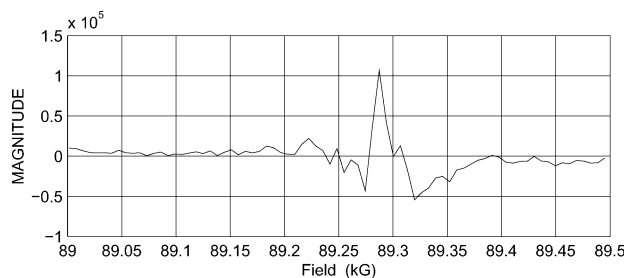
isotropic rotation constant of $R_{bar} = 5.3 \times 10^4$ s^{-1} and a Lorentzian width of 2 Gs (Figure 17). The time scale of molecular dynamics is suited to probing subnanosecond motions, or "fast" snapshots; in addition, in the current simulations there is no model for protein motion, which corresponds to the high-field experimental case. Using molecular dynamics data, with a high number of averages over initial conditions (10 000 random rotation matrices), high-field spectra have been simulated for both mutants (Figure 18). Extending the total time scale, and more averaging, are future directions for quality improvement. A few experimental ESR spectra on single-cysteine T4 mutants are presented in Figure 19 for comparison. For the particular N40C and K48C mutants that form the subject of the current analysis, only low-field spectra have been published;[7] however, high-field spectra are available for another pair of T4 variants,[39] studied for similar purposes (to infer from experiment and simulations the origin of differences in local mobilities, at sites 72 and 131):
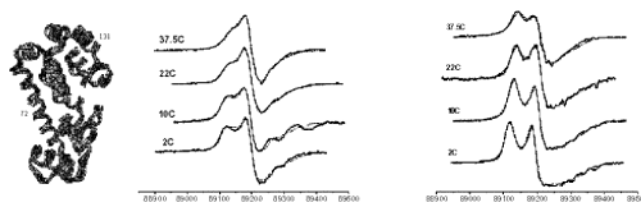
Figure 19. 250 GHz EPR spectra of T4 variants 72 (left) and 131 (right).[39]

4. Conclusions

Molecular dynamics trajectories provide a detailed description of the nitroxide moiety dynamics, at atomic resolution, and on a picosecond time scale (well suited for high-field ESR experiments). Restrictions in the rotational motions of the spin probe arise naturally from forces between the spin probe atoms and the neighboring protein residues, as well as the solvent molecules, all of which offer a more realistic description as compared to diffusion models with empirical parameters. However, the existing diffusion models offer a good approximation: results of the present MD simulations suggest that the

Figure 18. N40C (left) and K48C (right) 250 GHz EPR spectra obtained from a 110 ns FID. Rotation matrices were extracted from 110 ns appended molecular dynamics trajectories; averages were performed over 10 000 random initial orientations.

ESR Spectra of T4 Lysozyme

J. Phys. Chem. B, Vol. 108, No. 5, 2004 **1781**

motion of the spin probe can be modeled as a restricted diffusion, with transition rates in the nanosecond range. The spin label exhibits a "fast mode" (tens of picoseconds) and (at least) one "slow mode" (hundreds of picoseconds to nanoseconds), corresponding to the spin probe exploring high-probability regions in the space of rotational degrees of freedom, and to transitions between these states, respectively.

Similar OPLS/AMBER sampling distributions are the most probable cause for the resulting ESR line shapes of N40C and K48C not to exhibit the spectral differences expected from experiment. Extending the AMBER force field simulations, which have better sensitivity to local dynamics, along with a model (such as Brownian dynamics) for all-protein motion, might be a future direction for the improvement of ESR line shapes. Finally, it should be emphasized that the use of EPR line shapes to investigate atomic motions still faces a number of obstacles.

(i) The spin label is large and therefore must be attached at the surface of the protein. As a result it is difficult to examine the motion of internal residues or the hydrophobic core.

(ii) The spin probe may be too flexible to study motions of the protein backbone; though R1 was traditionally used in EPR experiments, recent results recommend other nitroxide-based probes, with shorter tethers, as better reporters of local flexibility.[7,9,24]

(iii) The highly averaged line shape may provide only limited information on internal dynamic modes. The computation of magnetic tensors from molecular dynamics trajectories is a femtosecond-time resolution procedure, whereas in actual EPR lines, the $\tilde{g}$ and $\tilde{A}$ tensors are averages over picosecond times. High-field EPR might thus be the method of choice for testing the theoretical predictions from molecular dynamics studies, because MD time scales are in the fast motion regime.

A. Appendix

The components of the irreducible Zeeman (magnetic) tensor are (β_e is the electron magnetic moment):

$$F_g^{(0,0)} = -\sqrt{\frac{1}{3}}\frac{2\pi\beta_e}{h}(g_{xx} + g_{yy} + g_{zz}) \qquad (L = 0, K = 0) \tag{33}$$

$$F_g^{(2,0)} = \sqrt{\frac{2}{3}}\frac{2\pi\beta_e}{h}\left(g_{zz} - \frac{g_{xx} + g_{yy}}{2}\right) \qquad (L = 2, K = 0) \tag{34}$$

$$F_g^{(2,\pm1)} = 0 \qquad (L = 2, K = \pm1) \tag{35}$$

$$F_g^{(2,\pm2)} = \frac{1}{2}\frac{2\pi\beta_e}{h}(g_{xx} - g_{yy}) \qquad (L = 2, K = \pm2) \tag{36}$$

The spin operator components for the Zeeman part are

$$A_g^{(0,0)} = -\sqrt{\frac{1}{3}}(\mathbf{B}_0 S_z) \qquad (L = 0, K = 0) \tag{37}$$

$$A_g^{(2,0)} = \sqrt{\frac{2}{3}}(\mathbf{B}_0 S_z) \qquad (L = 2, K = 0) \tag{38}$$

$$A_g^{(2,\pm1)} = \mp\frac{1}{2}(S_\pm \mathbf{B}_0) \qquad (L = 2, K = \pm1) \tag{39}$$

$$A_g^{(2,\pm2)} = 0 \qquad (L = 2, K = \pm2) \tag{40}$$

For the hyperfine interaction, the tensor operators and the spin operator components are respectively

$$F_A^{(0,0)} = -\sqrt{\frac{1}{3}}\frac{2\pi\beta_e g_{iso}}{h}(A_{xx} + A_{yy} + A_{zz}) \qquad (L = 0, K = 0) \tag{41}$$

$$F_A^{(2,0)} = \sqrt{\frac{2}{3}}\frac{2\pi\beta_e g_{iso}}{h}\left(A_{zz} - \frac{A_{xx} + A_{yy}}{2}\right) \qquad (L = 2, K = 0) \tag{42}$$

$$F_A^{(2,\pm1)} = 0 \qquad (L = 2, K = \pm1) \tag{43}$$

$$F_A^{(2,\pm2)} = \frac{1}{2}\frac{2\pi\beta_e g_{iso}}{h}(A_{xx} - A_{yy}) \qquad (L = 2, K = \pm2) \tag{44}$$

and

$$A_A^{(0,0)} = -\sqrt{\frac{1}{3}}\left(I_z S_z + \frac{1}{2}(S_+ I_- + S_- I_+)\right) \qquad (L = 0, K = 0) \tag{45}$$

$$A_A^{(2,0)} = \sqrt{\frac{2}{3}}\left(I_z S_z - \frac{1}{4}(S_+ I_- + S_- I_+)\right) \qquad (L = 2, K = 0) \tag{46}$$

$$A_A^{(2,\pm1)} = \mp\frac{1}{2}(S_\pm I_z + S_z I_\pm) \qquad (L = 2, K = \pm1) \tag{47}$$

$$A_A^{(2,\pm2)} = \frac{1}{2}(S_\pm I_\pm) \qquad (L = 2, K = \pm2) \tag{48}$$

where, as usual, $S_\pm$ and $I_\pm$ are the electron (S) and nuclear (I) spin raising and lowering operators.

References and Notes

(1) Freed, J. H. *Annu. Rev. Phys. Chem.* **2000**, *51*, 655−689.
(2) Borbat, P. P.; Freed, J. H. *Chem. Phys. Lett.* **1999**, *313*, 145−154.
(3) Borbat, P. P.; Costa-Filho, A. J.; Earle, K. A.; Moscicki, J. K.; Freed, J. H. *Science* **2001**, *291*, 266−269.
(4) Liang, Z. C.; Freed, J. H. *J. Phys. Chem. B* **1999**, *103*, 6384−6396.
(5) Columbus, L.; Hubbell, W. L. *Trends Biochem. Sci.* **2002**, *27*, 288−295.
(6) Columbus, L.; Kalai, T.; Jeko, J.; Hideg, L.; Hubbell, W. L. *Biochemistry* **2002**, *40*, 3828−3846.
(7) Mchaourab, H. S.; Lietzow, M. A.; Hideg, K.; Hubbell, W. L. *Biochemistry* **1996**, *35*, 7692−7704.
(8) Barnes, J.; Liang, Z.; Mchaourab, H. S.; Freed, J. H.; Hubbell, W. L. *Biophys. J.* **1999**, *76*, 3298−3306.
(9) Mchaourab, H. S.; Kalai, T.; Hideg, K.; Hubbell, W. L. *Biochemistry* **1999**, *38*, 2947−2955.
(10) Mchaourab, H. S.; Oh, K. J.; Fang, C. J.; Hubbell, W. L. *Biochemistry* **1997**, *36*, 307−316.
(11) Hubbell, W. L.; Altenbach, C.; Hubbell, C. M.; Khorana, H. G. *Adv. Protein Chem.* **2003**, *63*, 243−290.
(12) Altenbach, C.; Cai, K. W.; Klein-Seetharaman, J.; Khorana, H. G.; Hubbell, W. L. *Biochemistry* **2001**, *40*, 15483−15492.
(13) Altenbach, C.; Klein-Seetharaman, J.; Cai, K. W.; Khorana, H. G.; Hubbell, W. L. *Biochemistry* **2001**, *40*, 15493−15500.
(14) Muhiuddin, I. P.; et al. *Biochemistry* **1999**, *38*, 7159−7167.
(15) Utschig, L. M.; et al. *Biochemistry* **1997**, *36*, 8548−8558.
(16) van der Est, A.; et al. *J. Phys. Chem. A* **2002**, *106*, 8531−8542.
(17) Semenov, A. Y.; et al. *J. Biol. Chem.* **2000**, *275*, 23429−23438.
(18) LaConte, L. E. W.; et al. *Biophys. J.* **2002**, *83*, 1854−1866.
(19) Hakansson, P.; Westlund, P. O.; Lindahl, E.; Edholm, O. *Phys. Chem. Chem. Phys.* **2001**, *3*, 5311−5319.

(20) Schwartz, L. J.; Stillman, A. E.; Freed, J. H. *J. Chem. Phys.* **1982**, *77*, 5410−5425.

(21) Polimeno, A.; Freed, J. H. *J. Phys. Chem.* **1995**, *99*, 10995−11006.

(22) Polimeno, A.; Moro, G. J.; Freed, J. H. *J. Chem. Phys.* **1995**, *102*, 8094−8106.

(23) Earle, K. A.; Budil, D. E.; Freed, J. H. *J. Phys. Chem.* **1993**, *97*, 13289−13297.

(24) Steinhoff, H. J.; Hubbell, W. L. *Biophys. J.* **1996**,*71*, 2201−2212.

(25) Usova, N.; Westlund, P. O.; Fedchenia, I. I. *J. Chem. Phys.* **1995**, *103*, 96−103.

(26) Usova, N.; Perssoni, L.; Westlund, P. O. *Phys. Chem. Chem. Phys.* **2000**, *2*, 2785−2793.

(27) Liang, Z.; Westlund, P. O. *J. Chem. Phys.* **1993**, *99*, 7090−7097.

(28) Ge, M.; Freed, J. H. *Biophys. J.* **1999**, *76*, 264−280.

(29) Liang, Z.; Freed, J. H.; Keyes, R. S.; Bobst, A. M. *J. Phys. Chem. B* **2000**, *104*, 5372−5381.

(30) Robinson, B. H.; Slutsky, L. J.; Auteri, F. P. *J. Chem. Phys.* **1992**, *96*, 2609−2616.

(31) MacKerell, A. D.; Wiorkiewicz-Kuczera, J.; Karplus, M. *J. Am. Chem. Soc.* **1995**, *117*, 11946.

(32) Elber, R.; et al. *Comput. Phys. Comm.* **1994**, *91*, 159−189.

(33) Jorgensen, W. L.; Tirado-Rives, J. *J. Am. Chem. Soc.* **1988**, *110*, 1657.

(34) Cornell, W. D.; et al. *J. Am. Chem. Soc.* **1995**, *117*, 5179−5197.

(35) Darden, T. A.; York, D. M.; Pedersen, L. G.*J. Chem. Phys.* **1993**, *98*, 10089−10092.

(36) Kabsch, W. *Acta Crystallogr. A* **1976**, *32*, 922−923.

(37) Stoica, I. Ph.D. Thesis, Cornell University, 2003.

(38) Freed, J. H. Theory of slow tumbling ESR spectra for nitroxides. *Spin labeling − Theory and applications*; Academic Press: New York, 1976; Chapter 3, pp 54−130.

(39) Liang, Z.; Lou, Y.; Freed, J. H.; Columbus, L.; Hubbell W. L. *ACERT Symposium Center Highlights* June, **2003**.